Seismic estimation of fluid saturation based on rock physics: A case study of the tight-gas sandstone reservoirs in Ordos Basin

Chao Li[1], Peng Hu[1], Jing Ba[1]*, José M. Carcione[1,2], Tianwen Hu[3], Mengqiang Pang[1]

1 School of Earth Sciences and Engineering, Hohai University, Nanjing 211100, P. R. China.
2 National Institute of Oceanography and Applied Geophysics (OGS), Trieste, Italy.
3 Geological Exploration & Development Research Institute of CCDC, CNPC, Chengdu 610056, China.

**Corresponding author*

ABSTRACT

Tight-gas sandstone reservoirs of the Ordos Basin of China are characterized by high rock-fragment content, dissimilar pore types and a random distribution of fluids, leading to strong local heterogeneity. We model the seismic properties of these sandstones with the double-double porosity (DDP) theory, which considers water saturation, porosity and the frame characteristics. A generalized seismic wavelet is used to fit the real wavelet and the peak frequency-shift method is combined with the generalized S-transform to estimate attenuation. Then, we establish rock-physics templates (RPTs) based on P-wave attenuation and impedance. We use the log data and related seismic traces to calibrate the RPTs and generate a 3D volume of rock-physics attributes for the quantitative prediction of saturation and porosity. The predicted values are in good agreement with the actual gas production reports, indicating that the method

can be effectively applied to heterogeneous tight-gas sandstone reservoirs.

Keywords: Tight-gas sandstone; double-double porosity theory (DDP); rock-physics template; fluid saturation; porosity; seismic attenuation.

INTRODUCTION

With the progress of hydrocarbon seismic exploration techniques worldwide, as well as the increasing demand for oil/gas resources, the development of new areas is based on lithological interpretation rather than mapping structures, and consider unconventional reservoirs (Schmoker, 2002; Lampe et al., 2015). Unconventional reservoirs cannot be properly identified by classical geophysical prospecting methods (Singh et al., 2008; Martin et al., 2010; Pang et al., 2021). Hence, new methods, mainly based on rock physics, are required to explore these new resources. In fact. reservoir rocks are composite fluid/solid systems. Biot (1956a, b) and Gassmann (1951) first proposed a poroelasticity theory for wave propagation in single-porosity media. White (1975) proposed a mesoscopic-loss theory to analyze wave propagation when the two pore fluids are immiscible. Berryman and Milton (1991) distinguished between equant pores and cracks to extend the Gassmann equation. Ba et al. (2011) derived a double-porosity model to describe wave propagation, by modeling the effects of mesoscale fluid distribution and frame inhomogeneity. More recently, Ba et al. (2017) presented a double-double porosity theory (DDP).

Amplitude-variations with offset (AVO) theories to detect bright spots in tight reservoirs also require new developments based on rock physics (Avseth et al., 2004; Carcione et al., 2015). Singha et al. (2017) use RPTs to estimate saturation in Raghavapuram shales and Gollapalli sandstones. Luo et al. (2019) improved the Xu-White model and established a tight sandstone rock-physics model by considering feldspar in the pores of deep sandstone reservoirs, to predict gas saturation and porosity. Pang et al. (2021) propose 3D RPTs to estimate oil saturation in Songliao Basin.

The choice of the fluid identification factor/attribute is the basis for reservoir fluid identification (Qiao et al., 2007). Wave attenuation (e.g., seismic quality factor, Q) has been considered to be one of the most sensitive factors (Quintal, 2012; Ba et al., 2017; Picotti et al., 2018), affected by lithology, porosity, etc. (Johnston et al., 1979; Rubino et al., 2012; Chabyshova et al., 2014). Partial saturation is one of the major causes of attenuation (Winkler et al., 1982). Xiong et al. (2011) used wave attenuation to predict zones of carbonate oolitic reservoirs, and Pang et al. (2019) used seismic Q to estimate porosity and fluid saturation in carbonates.

Tight-oil/gas sandstones oil/gas have a great exploration potential (Fan et al., 2019), specifically lithic sandstones (Zou et al., 2012). The latest resource assessment in China shows that oil/gas resources of tight clastic rocks of the four major basins in central and western China account for 45.3% of the total clastic rock resources. Because of the high rock-fragment content and diverse pore types of lithic sandstones, "sweet-spots" differ from that of conventional quartz sandstones (Qiao et al., 2019), i.e., the classical wave-propagation models cannot effectively be used to estimate saturation and porosity.

We establish a lithic-sandstone model by using the DDP theory and RPTs at seismic frequencies, based on well-log calibration. A 3D data volume of water saturation and porosity is then obtained.

OVERVIEW OF THE S AREA

Geological structure

The structural features of the Ordos basin are generally considered as an asymmetric dustpan-shaped syncline which is gentle in the east and steep in the west. According to the basement properties, geological evolution history and structural characteristics, the basin can be divided into six structural units: Yimeng uplift, Weibei uplift, Jinxi flexural fold belt, Yishan slope, Tianhuan depression and western margin thrust belt (Figure 1a). The S area is located on the structural unit of the Yishan slope in the northern central belt of the Ordos basin. It is a monocline structure. The total S area is about 900 km^2. The tectonic movement in the area is stable, and faults and uplifts are not developed. There are only several rows of low and gentle uplifts overturning from northeast to southwest on the slope.

Stratigraphic lithology

The reservoirs are tight-gas sandstone reservoirs of the Upper Paleozoic formations with a burial depth between 2.9 and 3.5 km. The lithology is mainly fluvial facies sedimentary lithic quartz and lithic sandstones. The volume content of quartz is high, ranging from 50% to 91%, the content of feldspar is low, with an average of 3%, and the average content of rock fragments is around 20% (Figure 1b). The mineral composition of the rock fragments is mainly quartz (bulk modulus 37 Gpa, shear modulus 44 Gpa and density 2650 Kg/m^3), feldspar (bulk modulus 37.5 Gpa, shear modulus 15 Gpa and density 2620 Kg/m^3), calcite (bulk modulus 76.8 Gpa, shear modulus 32 Gpa and density 2710 Kg/m^3), pyrite (bulk modulus 138.6 Gpa, shear modulus 109.8 Gpa and density 4930 Kg/m^3) and clay (bulk modulus 21 Gpa, shear modulus 7 Gpa and density 2600 Kg/m^3) (Mavko et al., 2009).

Pore structure

Through thin section analysis, it is shown that the pore types are mainly secondary, such as intergranular dissolution, miscellaneous base holes, intergranular and intragranular dissolved pores of rock fragments (see Figure 2). Intergranular dissolution pores (Figure 3a) are generated by the dissolution of intergranular cements and exhibit good connectivity. Miscellaneous base holes are tiny pores left by the intergranular fillings, not completely compacted in the process of deposition. Intragranular dissolved pores of dispersed rock fragments can be seen in Figure 3b. Finally, intergranular pores (Figure 3c) are most common. The distribution of reservoir porosity ranges from 2% to 12%, the main fluids are gas and water, and the permeability ranges from 0 to 1 mD.

ROCK-PHYSICS MODEL

Considering that the rocks have a high rock-fragment content and complex pore structures, we adopt a double-double pore structure to model the wave properties. Figure 4 shows the lithic-sandstone rock-physics workflow. The process is as follows:

a. Mineral mixture: The mixture of quartz and feldspar is the solid of the host skeleton and the rock fragments are the embedded inclusions. The SCA model (Berryman, 1980) is used to obtain the bulk and shear moduli of the mixture:

$$\sum x_i(K_i - K^*_{SC})P^{*i} = 0, \tag{1a}$$

$$\sum x_i(\mu_i - \mu^*_{SC})Q^{*i} = 0, \tag{1b}$$

where x_i is the volume fraction of each component, P^{*i} and Q^{*i} are geometrical factors of the i-th component, K_i/μ_i are their bulk/shear moduli, and K^*_{SC} and μ^*_{SC} are the effective bulk and shear moduli, respectively.

b. Dry-rock skeleton: The intergranular dissolution pores, intergranular pores and miscellaneous base holes are assumed to constitute the pore space of host skeleton, and the intragranular dissolved pores of rock fragments are the pores of the inclusions. The pore space of the inclusions account for 20% of the total porosity. The DEM model (Berryman, 1992) is used to add the two types of pores into the host matrix and inclusion matrix, respectively:

$$(1-y)\frac{\mathrm{d}}{\mathrm{dy}}[K^*(y)] = (K_2 - K^*)P^{(*2)}(y), \tag{2a}$$

$$(1-y)\frac{\mathrm{d}}{\mathrm{dy}}[\mu^*(y)] = (\mu_2 - \mu^*)Q^{(*2)}(y), \tag{2b}$$

where $K^*(0) = K_1$, and $\mu^*(0) = \mu_1, K_1/\mu_1$ and K_2/μ_2 represent the bulk/shear moduli of the host and inclusions, respectively, y is the content of inclusions, and P and Q are geometric factors.

c. Patchy saturated rock: The dry rock has two components, each patchy saturated, both containing both water and gas. Each component can be considered a secondary double-porosity structure. The DDP theory, which characterizes four kinds of pore structure, is used to perform the fluid substitution. The bulk modulus, density and viscosity of water and gas are 2.34 GPa, 945 Kg/m^3, and 0.0018 Pa s, and 0.081 GPa, 204 Kg/m^3, and 0.000028 Pa s, respectively, which were calculated by using the equations proposed by Batzle and Wang (1992). The equations of the DDP theory are solved for plane waves to obtain the velocity and attenuation (Carcione, 2014)

$$V_P = \left[\mathrm{Re}(v^{-1}) \right]^{-1}, \tag{3a}$$

$$Q = \frac{\mathrm{Re}(v^2)}{\mathrm{Im}(v^2)}, \tag{3b}$$

where $v = \omega / k$ is the complex velocity, k is the complex wave number obtained by the plane-wave solutions (see Appendix A-1), and ω is the angular frequency.

WAVE RESPONSE

We analyze the P-wave velocity and dissipation factor (inverse of Q) as a function of frequency, inclusion content (rock-fragment content), porosity and water saturation.

Figure 5 shows the effect of the inclusion content as a function of frequency, for full water saturation and a porosity of 12%. Increasing rock-fragment content, attenuation and dispersion increase and the relaxation peak is located at the seismic band.

Figures 6 and 7 show the P-wave impedance and dissipation factor as a function of water saturation and porosity. The content of rock fragments is set to 20%. Impedance increases with saturation and decreases with porosity, with the latter trend more pronounced. Increasing porosity, attenuation increases and shows a peak at approximately 90% water saturation, as verified in early reported experiments and theoretical predictions (e.g., Yin et al., 1992; Carcione et al., 2006).

ROCK-PHYSICS TEMPLATE

The RPT is built as in Figure 8, with isolines of water saturation and porosity. The frequency is 35 Hz and the porosity and water saturation are set as variables.

SEISMIC ATTENUATION

Source wavelet

The spectral-ratio method is widely used for Q-factor estimation (Toksóz et al., 1979), which is obtained from the logarithm of the amplitude spectrum ratio of a reference wave and the actual wave. Quan and Harris (1997) proposed the centroid frequency-shift method by assuming that the source wavelet spectrum has Gaussian, box or triangular shapes. Zhang and Ulrych (2002) assumed a Ricker wavelet, where Q is obtained from the shift in peak frequency from source to receiver. Here, we use the generalized seismic wavelet (GSW) to fit the real signal (Wang et al.,2015):

$$\phi^{(u)}(\omega)=\left(\frac{u}{2}\right)^{-\frac{u}{2}}\frac{\omega^u}{\omega_0^u}\exp\left(-\frac{\omega^2}{\omega_0^2}+\frac{u}{2}\right), \tag{4}$$

where u is a shape factor which controls the symmetry property and ω_0 is the dominant angular frequency. Then, Q is obtained as in Wang et al. (2018). Since the robustness of the peak frequency-shift method is affected for low signal-to-noise ratio, we consider an average peak frequency

$$\omega_P=\frac{\omega_0^2}{4}\left(\sqrt{\frac{\tau^2}{4Q^2}+\frac{8u}{\omega_0^2}}-\frac{\tau}{2Q}\right), \tag{5}$$

where τ is a travel time, and

$$Q=\frac{\tau\omega_0^2\omega_P}{2\left(u\omega_0^2-2\omega_P^2\right)}. \tag{6}$$

By setting the derivative of equation (4) to zero, we obtain

$$\omega_P=\omega_0\sqrt{\frac{u}{2}}. \tag{7}$$

By substituting this expression into equation (6), the quality factor becomes

$$Q=\frac{\pi\tau f_0^2 u f_r\sqrt{\frac{u_r}{2}}}{2\left(uf_0^2-u_r f_r^2\right)}, \tag{8}$$

where f_0 and f_r are reference frequencies of the source wavelet and the attenuated wave at the receiver, respectively, and u, f_0, u_r, and f_r are obtained from equation (4) fitting the source wavelet and the attenuated waveform, respectively.

Time-frequency analysis method

Reine et al.（2009）obtained amplitude spectra with the short-time Fourier, Gabor, ST, and continuous wavelet transforms to compute *Q*, and concluded that the time-frequency transform method based on a variable time window is more robust than that obtained by the time-frequency transform with a fixed time window. Liu et al. (2017) reduced the effect of the time window caused by the time-frequency analysis, by adopting the S-transform proposed by Stockwell et al. (1996):

$$S(z,f)=\int_{-\infty}^{\infty}h(t)\frac{|f|}{\sqrt{2\pi}}\mathrm{e}^{-\frac{(t-z)^2f^2}{2}}\mathrm{e}^{-\mathrm{i}2\pi ft}\mathrm{d}t, \tag{9}$$

where z gives the position of the wavelet, $h(t)$ is the time domain signal and f is the frequency. In order to handle different non-stationary seismic signals, Chen et al. (2009) redefined the window function and proposed the generalized S transform. This function is

$$g(t)=\frac{\lambda|f|^p}{\sqrt{2\pi}}e^{-\frac{\lambda^2t^2|f|^{2p}}{2}}. \tag{10}$$

By adjusting the parameters of λ and P, an optimal fit of the real signal can be obtained.

Time-frequency characteristics

We use the generalized S-transform to analyze the time-frequency characteristics of the seismogram shown in Figure 9a, that goes through three wells with different gas production (moderate, dry and high). Figures 9b, c and d show the frequency sections at 20 Hz, 30 Hz and 40 Hz, respectively. The dominant frequency of the data is approximately 35 Hz. There is a strong low-frequency anomaly below the high-production reservoir at 20 Hz, while at higher frequencies this anomaly is weak, and other strong events appear, mainly at the dry-well location. This analysis indicates that low-frequency anomalies may be used to identify high gas-bearing reservoirs.

Estimation of attenuation

The source wavelet is extracted from seismic data. Figure 10a shows post-stack data, and Figure 10b shows the extracted source wavelet from 1.5 to 1.8 s, which is transformed to the frequency domain and fitted by equation (4) (see Figure 10c). Figure 11a and b show a single seismic trace and the amplitude spectrum from 1.8 to 2.3 s obtained with the generalized S transform, respectively. Equation (4) is used to fit the spectrum (Figure 11c), and equation (8) to compute Q.

Figures 12 and 13 show the amplitude profiles of the 2D seismic lines, and the corresponding attenuation profiles, where attenuation anomalies can be observed around wells A1 and C2.

TEMPLATE CALIBRATION

The template is calibrated with well-log data, and the estimated P-wave attenuation and P-wave impedance near the wells.

Figures 14 and 15 compare the RPTs at the well locations, with the reservoir porosity and water saturation obtained from the of logs (symbols). The reservoir lithology varies laterally due to heterogeneity between the two wells, and consequently, there is a difference between the two RPTs. Indeed, a single RPT is not able to describe the in-situ reservoir characteristics of the whole area. Thus, several wells with high gas or water production are considered to obtain the RPTs. A 3D data volume of rock-physics model can then be derived by the optimization method (Hao et al., 2016) to estimate porosity and saturation.

Single calibrated RPT can be expressed by M_k, with k denoting the k-th well. Rock-physics models are built at each set of coordinates (x,y) in the area. Their determination relies on the calibrated RPTs at each well location as

$$M_{3D}(x,y)=\sum_{k=1}^{L} M_k * A(x,y,k), \tag{11}$$

where L is the number of wells and $A(x,y,k)$ is the weight coefficient of the k-th well which is used to obtain the RPT at (x, y).

$$A(x,y,k)=\frac{\dfrac{1}{(x-x_k)^2+(y-y_k)^2}}{\sum_{k'=1}^{L}\dfrac{1}{(x-x_{k'})^2+(y-y_{k'})^2}}, \text{ if } x\neq x_k,\ \ y\neq y_k, \tag{12}$$

where (x_k, y_k) is the coordinate of the k-th well.

RESULTS OF THE S AREA

Estimation from of 2D profiles

Figure 16 shows the P-wave impedances of the two 2D seismic survey lines. Figures

17 and 18 show the estimation along two 2D seismic lines. The first is a north-south section in the western zone of the S area, and the geologic structure rises gradually from north to south. Porosity and saturation at well A1 are both low. The water-saturated layers around well B1 exhibit continuous features, and the porosity of the upper part is higher than that of the lower part. Gas saturation at well C1 is high. According to reports, well A1 produces gas at 2.39×10^4 m^3 per day and water at 13.3 tons per day, well B1 produces water at 38.3 tons per day, and well C1 gas at 30.92×10^4 m^3 per day. The estimations agree with the production data.

The line in Figure 18 is an east-west section in the middle zone of S area. The estimated porosity at well A2 is high, which provides favorable conditions for gas accumulation, and the corresponding gas saturation is high. On the other hand, well C2 shows high water saturation. The gas production of well A2 is 104.26×10^4 m^3 per day. Well C2 produces gas 2.2×10^4 m^3 per day and water 64.8 tons per day. Well B2 produces gas at 1.91×10^4 m^3 per day and water at 10.8 tons per day. The estimations generally agree with the production data.

3D estimation

Figures 19 and 20 show the 3D estimations of porosity and water saturation (Gaussian filter is used for smoothing), respectively. Most of the gas wells are distributed at the locations with high porosity, favouring gas accumulation. The saturation estimations agree with the location of the water and gas wells, i.e., high and low water saturation, respectively. By comparing the production reports of the 26 wells with the estimations, the agreement is 84.6% (22 wells). The gas saturation in the northeast and southwest zones is higher, which also agrees with the geological reports.

CONCLUSION

This study analyzes the characteristics of lithic sandstone reservoirs of the S area in Ordos Basin (China). We use the SCA to model the effects of the rock fragments and other minerals to obtain the mineral mixture properties, and the DEM model to obtain the dry-rock moduli, based on two pore types. The complexity of the gas-water distribution is handled with the double-double porosity to obtain the wave properties, i.e., P-wave velocity, impedance and dissipation as a function of porosity and water saturation. A generalized seismic wavelet, the peak frequency-shift method and the generalized S transform, are used to estimate the attenuation. Then, rock-physics templates (RPT), calibrated with log data, are built to obtain these properties from seismic data. Several wells are considered to obtain RPTs at each well location, due to strong lateral heterogeneity variations. 2D and 3D maps of porosity and water saturation are then obtained from seismic data, where the results agree with production reports data.

ACKNOWLEDGEMENTS

This work is supported by the National Natural Science Foundation of China (grant no. 41974123), the Jiangsu Innovation and Entrepreneurship Plan and the Jiangsu Province Science Fund for Distinguished Young Scholars (grant no. BK20200021).

APPENDIX A

Plane-wave solutions

By substituting a plane P-wave kernel into differential equations of DDP theory, we compute the complex wave number k from

$$\begin{vmatrix} a_{11}k^2+b_{11} & a_{12}k^2+b_{12} & a_{13}k^2+b_{13} & a_{14}k^2+b_{14} & a_{15}k^2+b_{15} \\ a_{21}k^2+b_{21} & a_{22}k^2+b_{22} & a_{23}k^2+b_{23} & a_{24}k^2+b_{24} & a_{25}k^2+b_{25} \\ a_{31}k^2+b_{31} & a_{32}k^2+b_{32} & a_{33}k^2+b_{33} & a_{34}k^2+b_{34} & a_{35}k^2+b_{35} \\ a_{41}k^2+b_{41} & a_{42}k^2+b_{42} & a_{43}k^2+b_{43} & a_{44}k^2+b_{44} & a_{45}k^2+b_{45} \\ a_{51}k^2+b_{51} & a_{52}k^2+b_{52} & a_{53}k^2+b_{53} & a_{54}k^2+b_{54} & a_{55}k^2+b_{55} \end{vmatrix} = 0, \quad \text{(A-1a)}$$

where,

$$a_{11}=A+2N+(Q_1\phi_2-Q_2\phi_1)M_0^{(12)}+(Q_1\phi_3-Q_3\phi_1)M_0^{(13)}+(Q_2\phi_4-Q_4\phi_2)M_0^{(24)},$$

$$a_{12}=Q_1+(Q_1\phi_2-Q_2\phi_1)M_1^{(12)}+(Q_1\phi_3-Q_3\phi_1)M_1^{(13)}+(Q_2\phi_4-Q_4\phi_2)M_1^{(24)},$$

$$a_{13}=Q_2+(Q_1\phi_2-Q_2\phi_1)M_2^{(12)}+(Q_1\phi_3-Q_3\phi_1)M_2^{(13)}+(Q_2\phi_4-Q_4\phi_2)M_2^{(24)},$$

$$a_{14}=Q_3+(Q_1\phi_2-Q_2\phi_1)M_3^{(12)}+(Q_1\phi_3-Q_3\phi_1)M_3^{(13)}+(Q_2\phi_4-Q_4\phi_2)M_3^{(24)},$$

$$a_{15}=Q_4+(Q_1\phi_2-Q_2\phi_1)M_4^{(12)}+(Q_1\phi_3-Q_3\phi_1)M_4^{(13)}+(Q_2\phi_4-Q_4\phi_2)M_4^{(24)},$$

$$a_{21}=Q_1+R_1\phi_2M_0^{(12)}+R_1\phi_3M_0^{(13)}, \quad a_{22}=R_1+R_1\phi_2M_1^{(12)}+R_1\phi_3M_1^{(13)},$$

$$a_{23}=R_1\phi_2M_2^{(12)}+R_1\phi_3M_2^{(13)}, \quad a_{24}=R_1\phi_2M_3^{(12)}+R_1\phi_3M_3^{(13)}, \quad a_{25}=R_1\phi_2M_4^{(12)}+R_1\phi_3M_4^{(13)},$$

$a_{31}=Q_2-R_2\phi_1M_0^{(12)}+R_2\phi_4M_0^{(24)},\quad a_{32}=-R_2\phi_1M_1^{(12)}+R_2\phi_4M_1^{(24)},$ (A-1b)

$a_{33}=R_2-R_2\phi_1M_2^{(12)}+R_2\phi_4M_2^{(24)},\ a_{34}=-R_2\phi_1M_3^{(12)}+R_2\phi_4M_3^{(24)},$

$a_{35}=-R_2\phi_1M_4^{(12)}+R_2\phi_4M_4^{(24)},\ a_{41}=Q_3-R_3\phi_1M_0^{(13)},\ a_{42}=-R_3\phi_1M_1^{(13)},\ a_{43}=-R_3\phi_1M_2^{(13)},$

$a_{44}=R_3-R_3\phi_1M_3^{(13)},\ a_{45}=-R_3\phi_1M_4^{(13)},$

$a_{51}=Q_4-R_4\phi_2M_0^{(24)},\ a_{52}=-R_4\phi_2M_1^{(24)},\ a_{53}=-R_4\phi_2M_2^{(24)},$

$a_{54}=-R_4\phi_2M_3^{(24)},\ a_{55}=R_4-R_4\phi_2M_4^{(24)},$

$b_{11}=-\rho_{00}\omega^2+\mathrm{i}\omega(b_1+b_2+b_3+b_4),\ b_{12}=-\rho_{01}\omega^2-\mathrm{i}\omega b_1,\ b_{13}=-\rho_{02}\omega^2-\mathrm{i}\omega b_2,$

$b_{14}=-\rho_{03}\omega^2+\mathrm{i}\omega b_3,\ b_{15}=-\rho_{04}\omega^2-\mathrm{i}\omega b_4,\ b_{21}=-\rho_{01}\omega^2-\mathrm{i}\omega b_1,\ b_{22}=-\rho_{11}\omega^2+\mathrm{i}\omega b_1,$

$b_{23}=b_{24}=b_{25}=0,\ b_{31}=-\rho_{02}\omega^2-\mathrm{i}\omega b_2,\ b_{33}=-\rho_{22}\omega^2+\mathrm{i}\omega b_2,\ b_{32}=b_{34}=b_{35}=0,$

$b_{41}=-\rho_{03}\omega^2-\mathrm{i}\omega b_3,\ b_{44}=-\rho_{33}\omega^2+\mathrm{i}\omega b_3,\ b_{42}=b_{43}=b_{45}=0,$

$b_{51}=-\rho_{04}\omega^2-\mathrm{i}\omega b_4,\ b_{55}=-\rho_{44}\omega^2+\mathrm{i}\omega b_4,\ b_{52}=b_{53}=b_{54}=0,$

where,

$$M_0^{(12)}=\frac{(Q_1\phi_2-Q_2\phi_1)/S_{12}+R_1\phi_2\phi_3(Q_1\phi_3-Q_3\phi_1)/(S_{12}S_{13})-R_2\phi_1\phi_4(Q_2\phi_4-Q_4\phi_2)/(S_{12}S_{24})}{1-(R_1\phi_2\phi_3)^2/(S_{12}S_{13})-(R_2\phi_1\phi_4)^2/(S_{12}S_{24})},$$

$$M_1^{(12)}=\frac{R_1\phi_2/S_{12}+\phi_2(R_1\phi_3)^2/(S_{12}S_{13})}{1-(R_1\phi_2\phi_3)^2/(S_{12}S_{13})-(R_2\phi_1\phi_4)^2/(S_{12}S_{24})},$$

$$M_2^{(12)}=\frac{-R_2\phi_1/S_{12}-\phi_1(R_2\phi_4)^2/(S_{12}S_{24})}{1-(R_1\phi_2\phi_3)^2/(S_{12}S_{13})-(R_2\phi_1\phi_4)^2/(S_{12}S_{24})},$$

$$M_3^{(12)}=\frac{-\phi_1\phi_2\phi_4R_1R_3/(S_{12}S_{13})}{1-(R_1\phi_2\phi_3)^2/(S_{12}S_{13})-(R_2\phi_1\phi_4)^2/(S_{12}S_{24})},$$

$$M_4^{(12)}=\frac{\phi_1\phi_2\phi_4R_2R_4/(S_{12}S_{24})}{1-(R_1\phi_2\phi_3)^2/(S_{12}S_{13})-(R_2\phi_1\phi_4)^2/(S_{12}S_{24})},$$

$M_0^{(13)}=(M_0^{(12)}R_1\phi_2\phi_3+\phi_3Q_1-\phi_1Q_3)/S_{13},M_1^{(13)}=(M_1^{(12)}R_1\phi_2\phi_3+\phi_3R_1)/S_{13},$ (A-1c)

$M_2^{(13)}=(M_2^{(12)}R_1\phi_2\phi_3)/S_{13},M_3^{(13)}=(M_3^{(12)}R_1\phi_2\phi_3-\phi_3R_1)/S_{13},$

$$M_4^{(13)} = (M_4^{(12)} R_1\phi_2\phi_3)/S_{13}, M_0^{(24)} = (-M_0^{(12)} R_2\phi_1\phi_4 + Q_2\phi_4 - Q_4\phi_2)/S_{24},$$

$$M_1^{(24)} = (-M_1^{1(2)} R_2\phi_1\phi_4)/S_{24}, M_2^{(24)} = (-M_2^{(12)} R_2\phi_1\phi_4 + R_2\phi_4)/S_{24},$$

$$M_3^{(24)} = (-M_3^{(12)} R_2\phi_1\phi_4)/S_{24}, M_4^{(24)} = (-M_4^{(12)} R_2\phi_1\phi_4 - R_2\phi_4)/S_{24},$$

$$S_{12} = \frac{\mathrm{i}\omega\eta_f^{(1)} R_{12}^2 \phi_1^2 \phi_2^2 \phi_{20}}{3(\phi_2 + \phi_4)\kappa_1} - \frac{\rho_f^{(1)} \omega^2 R_{12}^2 \phi_1^2 \phi_2^2 \phi_{20}}{3\phi_{10}(\phi_2 + \phi_4)} - (\phi_2^2 R_1 + \phi_1^2 R_2),$$

$$S_{13} = \frac{\mathrm{i}\omega\eta_f^{(1)} R_{13}^2 \phi_1^2 \phi_3 \phi_{10}}{3\kappa_1} - \frac{\rho_f^{(1)} \omega^2 R_{13}^2 \phi_1^2 \phi_3}{3} - (\phi_3^2 R_1 + \phi_1^2 R_3),$$

$$S_{24} = \frac{\mathrm{i}\omega\eta_f^{(1)} R_{24}^2 \phi_2^2 \phi_4 \phi_{20}}{3\kappa_2} - \frac{\rho_f^{(1)} \omega^2 R_{24}^2 \phi_2^2 \phi_4}{3} - (\phi_4^2 R_2 + \phi_2^2 R_4).$$

REFERENCES

Avseth, P. A., and E. Odegaard, 2004, Well log and seismic data analysis using rock physics templates: First Break, **22**, doi: 10.3997/1365-2397.2004017.

Ba, J., J. M. Carcione, and J. X. Nie, 2011, Biot-Rayleigh theory of wave propagation in double-porosity media: Journal of Geophysical Research-Solid Earth, **116**, B06202, doi: 10.1029/2010jb008185.

Ba J., H. Cao, J. M. Carcione, G. Tang, X.-F. Yan, W.-t. Sun, and J.-x. Nie, 2013, Multiscale rock-physics templates for gas detection in carbonate reservoirs: Journal of Applied Geophysics, **93**, 77-82, doi: 10.1016/j.jappgeo.2013.03.011

Ba, J., W. H. Xu, L. Y. Fu, J. M. Carcione, and L. Zhang, 2017, Rock anelasticity due to patchy saturation and fabric heterogeneity: A double double-porosity model of wave propagation: Journal of Geophysical Research-Solid Earth, **122**, 1949-1976, doi: 10.1002/2016jb013882.

Berryman, J. G., 1980, Long-wavelength propagation in composite elastic media II. Ellipsoidal inclusions: Acoustical Society of America Journal, **68**, 1820-1831, doi: 10.1121/1.385172.

Berryman, J. G., 1992, Single-scattering approximations for coefficients in Biot’s equations of poroelasticity: Acoustical Society of America Journal, **91**, 551-571, doi: 10.1121/1.402518.

Berryman, J. G., and G. W. Milton, 1991, Exact results for generalized Gassmann's equations in composite porous media with two constituents: Geophysics, **56**, 1950-1960, doi: 10.1190/1.1443006.

Biot, M. A., 1956a, Theory of Propagation of Elastic Waves in a Fluid‐Saturated Porous Solid. I. Low‐Frequency Range: Acoustical Society of America Journal, **28**, 168-178, doi: 10.1121/1.1908239.

Biot, M. A., 1956b, Theory of Propagation of Elastic Waves in a Fluid‐Saturated Porous Solid. II. Higher Frequency Range: Acoustical Society of America Journal, **28**, 179-191, doi: 10.1121/1.1908241.

Carcione, J. M., 2014, Wave fields in real media, Theory and numerical simulation of wave propagation in anisotropic, anelastic, porous and electromagnetic media (Third edition): Elsevier.

Carcione, J. M., and P. Avseth, 2015, Rock-physics templates for clay-rich source rocks: Geophysics, **80**, D481-D500, doi: 10.1190/geo2014-0510.1.

Carcione, J. M., S. Picotti, D. Gei, and G. Rossi, 2006, Physics and Seismic Modeling for Monitoring CO2 Storage: pure and applied geophysics, **163**, 175-207, doi: 10.1007/s00024-005-0002-1.

Chabyshova, E., and G. Goloshubin, 2014, Seismic modeling of low-frequency "shadows" beneath gas reservoirs: Geophysics, **79**, D417-D423, doi: 10.1190/geo2013-0379.1.

Chen, X. H., Z. H. He, D. J. Huang, and X. T. Wen, 2009, Low frequency shadow detection of gas reservoirs in time-frequency domain: Chinese Journal of Geophysics-Chinese Edition, **52**, 215-221.

Fan, A. P., R. C. Yang, N. Lenhardt, M. Wang, Z. Z. Han, J. B. Li, Y. J. Li, and Z. J. Zhao, 2019, Cementation and porosity evolution of tight sandstone reservoirs in the Permian Sulige gas field, Ordos Basin (central China): Marine and Petroleum Geology, **103**, 276-293, doi: 10.1016/j.marpetgeo.2019.02.010.

Gassmann F., 1951, “Uber die Elastizitat Poroser Medien,” Veirteljahrsschrift der Naturforschenden Gesellschaft in Zzirich, **96**, 1-23.

Hao Z., J. Ba, L. Zhang, Q. Zeng, R. Jiang, J. Liu, W. Qian, W. Tan, and W. Cheng, 2016, Rock physics inversion workflow on reservoir parameters: a case study of seismic hydrocarbon detection in large-area tight dolomite reservoirs: Journal of Seismic Exploration, **25**, 561-588.

Johnston, D. H., M. N. Toksoz, and A. Timur, 1979, Attenuation of seismic waves in dry and saturated rocks; II, Mechanisms: Geophysics, **44**, 691-711, doi:

10.1190/1.1440970.

Liu N., B. Zhang, H. Wu, and J. Gao, 2017, Q estimation from time-migrated gathers based on S transform: SEG Technical Program Expanded Abstracts, 3499-3504, doi: 10.1190/segam2017-17790238.1

Luo, Y. N., H. D. Huang, M. Jakobsen, Y. D. Yang, J. W. Zhang, and Y. J. Cai, 2019, Prediction of porosity and gas saturation for deep-buried sandstone reservoirs from seismic data using an improved rock-physics model: Acta Geophysica, **67**, 557-575, doi: 10.1007/s11600-019-00274-6.

Lampe, D. J., and J. F. Stolz, 2015, Current perspectives on unconventional shale gas extraction in the Appalachian Basin: Journal of Environmental Science and Health Part a-Toxic/Hazardous Substances & Environmental Engineering, **50**, 434-446, doi: 10.1080/10934529.2015.992653.

Martin, S. O. O., S. A. A. Holditch, W. B. B. Ayers, and D. A. A. McVay, 2010, PRISE Validates Resource Triangle Concept: SPE Economics & Management, **2**, 51-60, doi: 10.2118/117703.

Mavko G., Mukerji T. and Dvorkin J. 2009. The Rock Physics Handbook: Tools for Seismic Analysis of Porous Media. Cambridge University Press.

Pang, M. Q., J. Ba, J. M. Carcione, S. Picotti, J. Zhou, and R. Jiang, 2019, Estimation of porosity and fluid saturation in carbonates from rock-physics templates based on seismic Q: Geophysics, **84**, M25-M36, doi: 10.1190/geo2019-0031.1.

Pang, M. Q., J. Ba, J. M. Carcione, L. Zhang, R. P. Ma, and Y. J. Wei, 2021, Seismic identification of tight-oil reservoirs by using 3D rock-physics templates: Journal of Petroleum Science and Engineering, **201**, 108476, doi: 10.1016/j.petrol.2021.108476.

Pang, X., X. Shao, M. Li, T. Hu, Z. Chen, K. Zhang, F. Jiang, J. Chen, D. Chen, J. Peng, B. Pang, and W. Wang, 2021, Correlation and difference between conventional and unconventional reservoirs and their unified genetic classification: Gondwana Research, **97**, 73-100, doi: 10.1016/j.gr.2021.04.011.

Picotti, S., J. M. Carcione, and J. Ba, 2018, Rock-physics templates based on seismic Q: Geophysics, **84**, MR13-MR23, doi: 10.1190/geo2018-0017.1.

Qiao, Y. D., and H. W. An, 2007, Study of petrophysical parameter sensitivity from well log data: Applied Geophysics, **4**, 282-287, doi: 10.1007/s11770-007-0038-3.

Qiao, J. C., J. H. Zeng, S. Jiang, S. Feng, X. Feng, Z. Guo, and J. L. Teng, 2019, Heterogeneity of reservoir quality and gas accumulation in tight sandstone reservoirs revealed by pore structure characterization and physical simulation: Fuel, **253**, 1300-1316, doi: 10.1016/j.fuel.2019.05.112.

Quan, Y., and J. M. Harris, 1997, Seismic attenuation tomography using the frequency shift method: Geophysics, **62**, 895-905, doi: 10.1190/1.1444197.

Quintal, B., 2012, Frequency-dependent attenuation as a potential indicator of oil saturation: Journal of Applied Geophysics, **82**, 119-128, doi: 10.1016/j.jappgeo.2012.03.001.

Reine, C., M. van der Baan, and R. Clark, 2009, The robustness of seismic attenuation measurements using fixed- and variable-window time-frequency transforms: Geophysics, **74**, WA123-WA135, doi: 10.1190/1.3043726.

Rubino, J. G., D. R. Velis, and K. Holliger, 2012, Permeability effects on the seismic response of gas reservoirs: Geophysical Journal International, **189**, 448-468, doi: 10.1111/j.1365-246X.2011.05322.x.

Schmoker, J. W., 2002, Resource-assessment perspectives for unconventional gas systems: Aapg Bulletin, **86**, 1993-1999.

Singh, K., S. A. Holditch, and W. B. Ayers, Jr., 2008, Basin Analog Investigations Answer Characterization Challenges of Unconventional Gas Potential in Frontier Basins: Journal of Energy Resources Technology-Transactions of the Asme, **130**, 043202, doi: 10.1115/1.3000104.

Singha, D. K., and R. Chatterjee, 2017, Rock physics modeling in sand reservoir through well log analysis, Krishna-Godavari basin, India: Geomechanics and Engineering, **13**, 99-117, doi: 10.12989/gae.2017.13.1.099.

Stockwell, R. G., L. Mansinha, and R. P. Lowe, 1996, Localization of the complex spectrum: The S transform: Ieee Transactions on Signal Processing, **44**, 998-1001, doi: 10.1109/78.492555.

Toksóz, M. N., D. H. Johnston, and A. Timur, 1979, Attenuation of seismic waves in dry and saturated rocks; I, Laboratory measurements: Geophysics, **44**, 681-690, doi: 10.1190/1.1440969.

Wang, Q., and J. H. Gao, 2018, An improved peak frequency shift method for Q estimation based on generalized seismic wavelet function: Journal of Geophysics and Engineering, **15**, 164-178, doi: 10.1088/1742-2140/aa8714.

Wang, Y. H., 2015, Generalized seismic wavelets: Geophysical Journal International, **203**, 1172-1178, doi: 10.1093/gji/ggv346.

White, J. E., 1975, Computed seismic speeds and attenuation in rocks with partial gas saturation: Geophysics, **40**, 224-232, doi: 10.1190/1.1440520.

Winkler, K. W., and A. Nur, 1982, Seismic attenuation: Effects of pore fluids and frictional-sliding: Geophysics, **47**, 1-15, doi: 10.1190/1.1441276.

Xiong, X. J., X. L. He, Y. Pu, Z. H. He, and K. Lin, 2011, High-precision frequency attenuation analysis and its application: Applied Geophysics, **8**, 337-343, doi: 10.1007/s11770-011-0302-4.

Yin, C.-S., M. L. Batzle, and B. J. Smith, 1992, Effects of partial liquid/gas saturation on extensional wave attenuation in Berea sandstone: **19**, 1399-1402, doi: 10.1029/92GL01159.

Zhang, C. J., and T. J. Ulrych, 2002, Estimation of quality factors from CMP records: Geophysics, **67**, 1542-1547, doi: 10.1190/1.1512799.

Zou, C., R. Zhu, K. Liu, L. Su, B. Bai, X. Zhang, X. Yuan, and J. Wang, 2012, Tight gas sandstone reservoirs in China: characteristics and recognition criteria: Journal of Petroleum Science and Engineering, **88-89**, 82-91, doi: 10.1016/j.petrol.2012.02.001.

LIST OF FIGURES

Figure 1. (a) Tectonic zoning map of Ordos Basin. (b) Ternary map of reservoir lithology of the target formations in the S area.

Figure 2. Pore-space distribution of rocks in the S area.

Figure 3. Scanning electron microscope images. (a) Intergranular dissolution pores, (b) intragranular dissolved pores of rock fragments, and (c) intergranular pores.

Figure 4. Rock-physics workflow.

Figure 5. Effect of the inclusion content (Ic) on P-wave velocity (a) and dissipation factor (b).

Figure 6. Effect of water saturation and porosity on P-wave impedance.

Figure 7. Effect of water saturation and porosity on P-wave attenuation.

Figure 8. RPT of tight-gas sandstones. The black and red curves represent isolines of water saturation and porosity.

Figure 9. Post-stack seismic section (a), and S-transforms at 20 Hz (b), 30 Hz (c), and 40 Hz (d).

Figure 10. Post-stack seismic data (a), seismic wavelet in the time domain (b), and source wavelet amplitude spectrum fit by the GSW equation (6) (c).

Figure 11. Single seismic trace (a), generalized S transform (b), and amplitude spectrum fit by the GSW equation (6) (c).

Figure 12. 2D seismic line crossing wells A1, B1 and C1. Amplitude (a) and attenuation

(b) profiles.

Figure 13. 2D seismic line crossing wells A2, B2 and C2. Amplitude (a) and attenuation (b) profiles.

Figure 14. Seismic rock-physics interpretation template around well A.

Figure 15. Seismic-rock physics interpretation template around well B.

Figure 16. 2D P-wave impedance profiles crossing (a) wells A1, B1 and C1, and (b) wells A2, B2 and C2.

Figure 17. 2D profiles crossing wells A1, B1 and C1. (a) Porosity and (b) water saturation.

Figure 18. 2D profiles crossing wells A2, B2 and C2. (a) Porosity and (b) water saturation.

Figure 19. 3D prediction of reservoir porosity (the blue dots indicate high water saturation, and red high gas saturation).

Figure 20. 3D prediction of water saturation (the blue dots indicate high water saturation, and red high gas saturation).

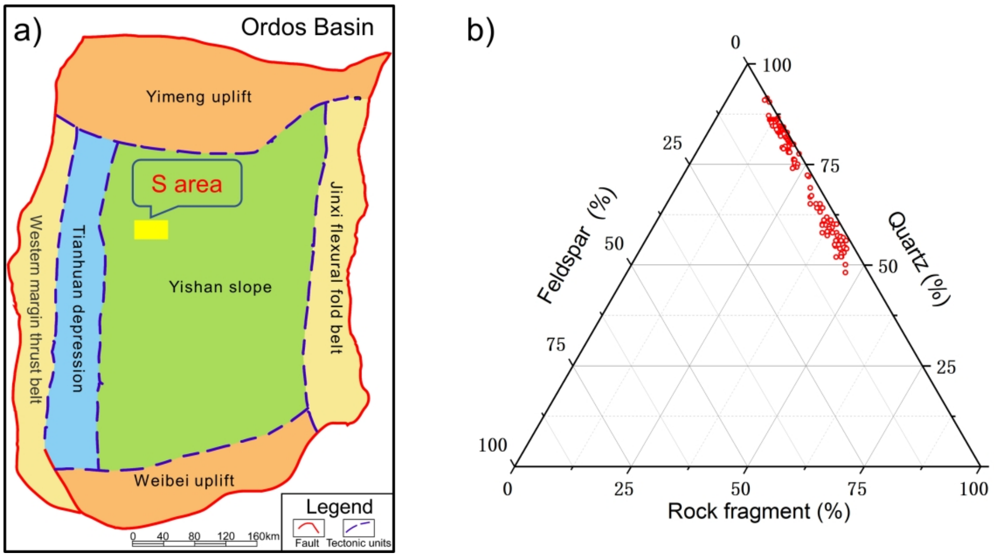

Figure 1. (a) Tectonic zoning map of Ordos Basin. (b) Ternary map of reservoir lithology of the target formations in the S area.

262x144mm (300 x 300 DPI)

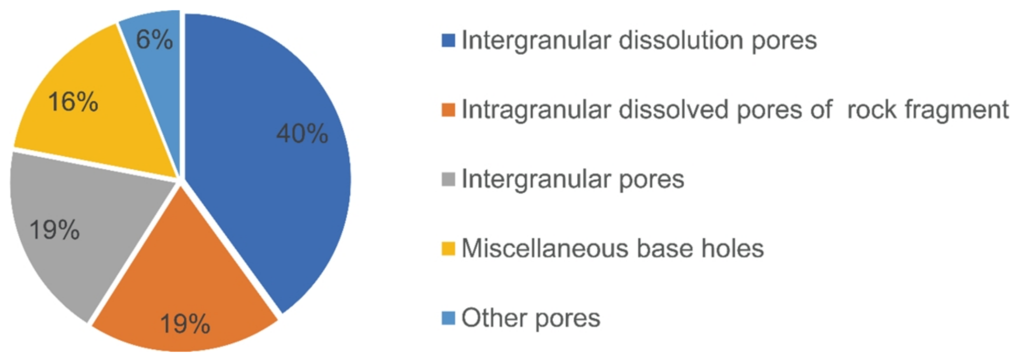

Figure 2. Pore-space distribution of rocks in the S area.

186x63mm (300 x 300 DPI)

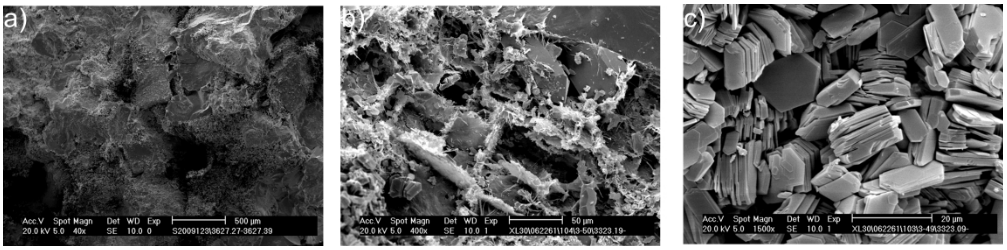

Figure 3. Scanning electron microscope images. (a) Intergranular dissolution pores, (b) intragranular dissolved pores of rock fragments, and (c) intergranular pores.

320x77mm (300 x 300 DPI)

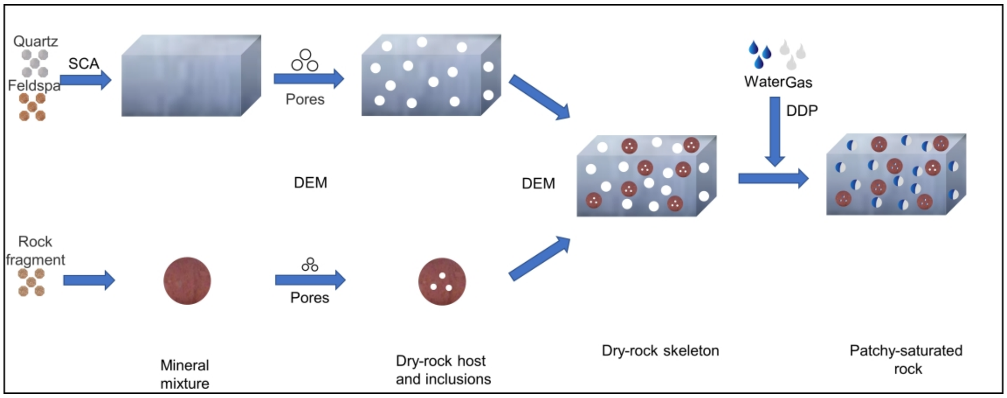

Figure 4. Rock-physics workflow.

325x126mm (300 x 300 DPI)

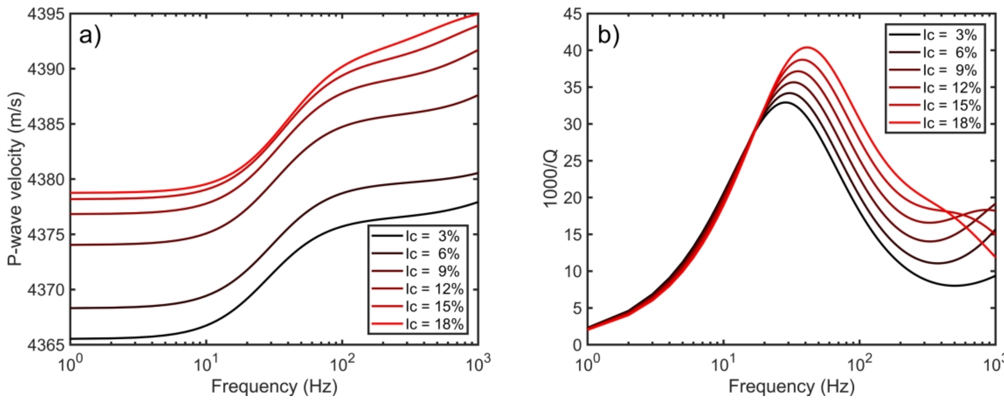

Figure 5. Effect of the inclusion content (Ic) on P-wave velocity (a) and dissipation factor (b).

338x131mm (300 x 300 DPI)

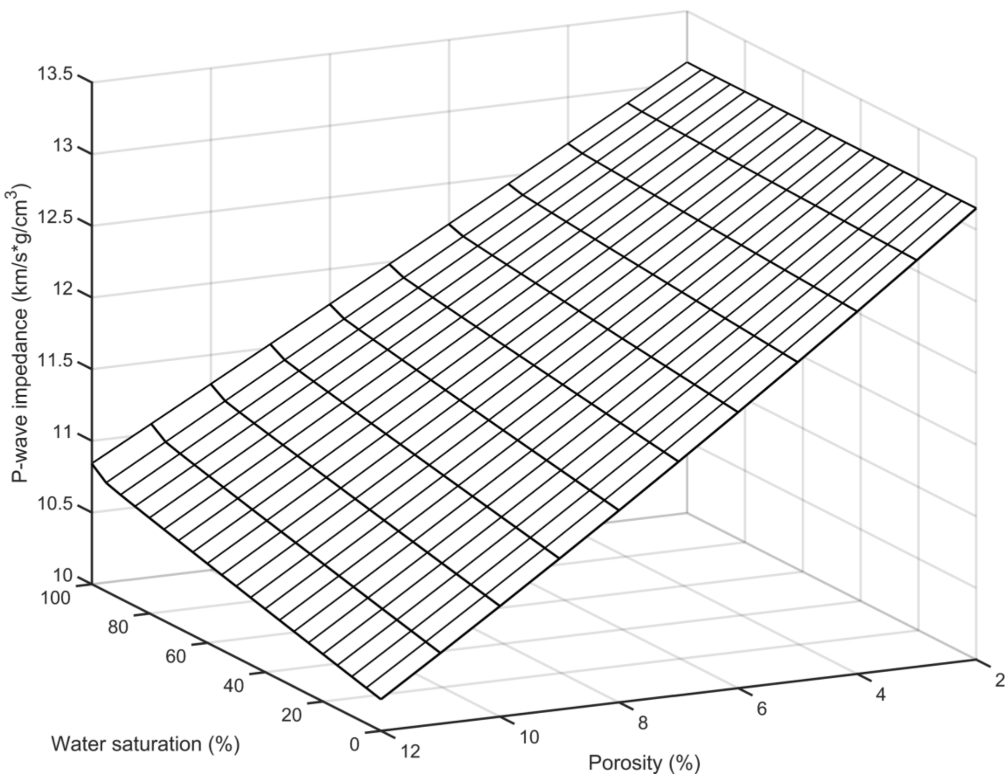

Figure 6. Effect of water saturation and porosity on P-wave impedance.

249x190mm (300 x 300 DPI)

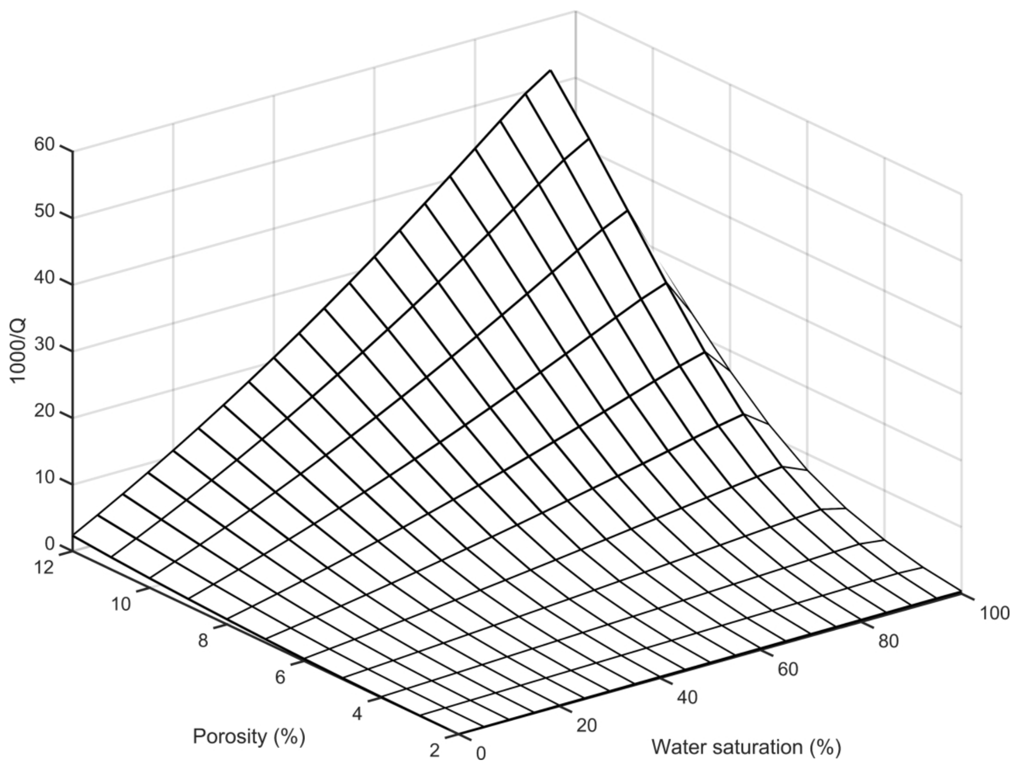

Figure 7. Effect of water saturation and porosity on P-wave attenuation.

253x190mm (300 x 300 DPI)

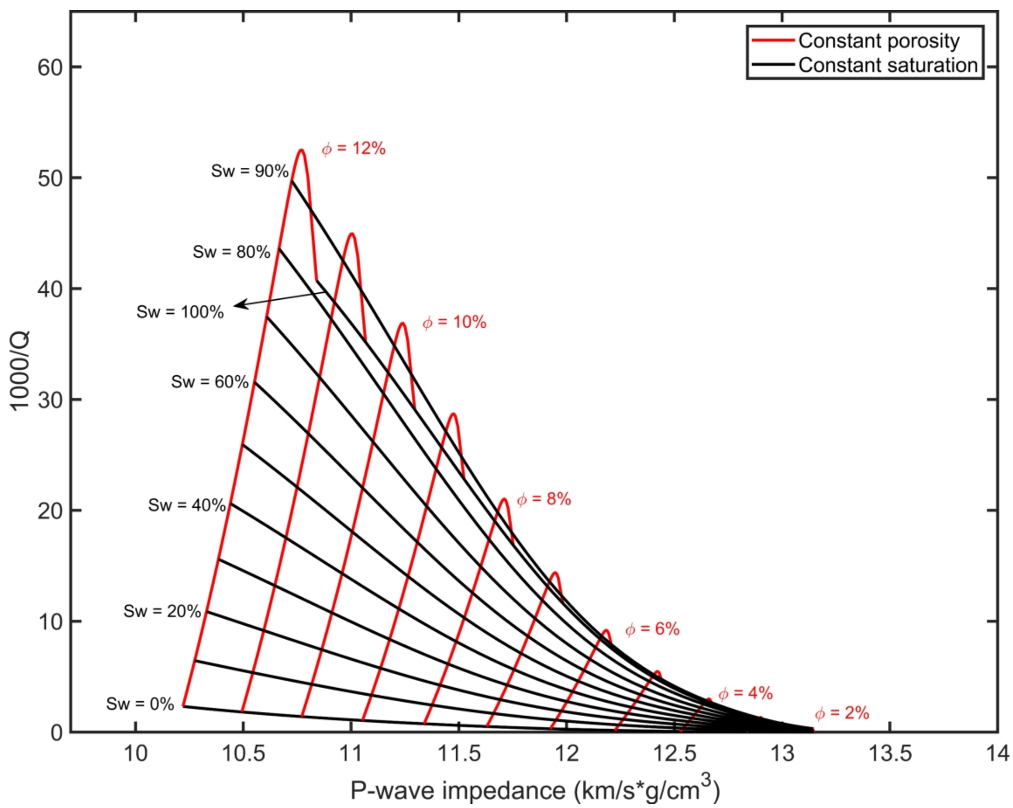

Figure 8. RPT of tight-gas sandstones. The black and red curves represent isolines of water saturation and porosity.

239x190mm (300 x 300 DPI)

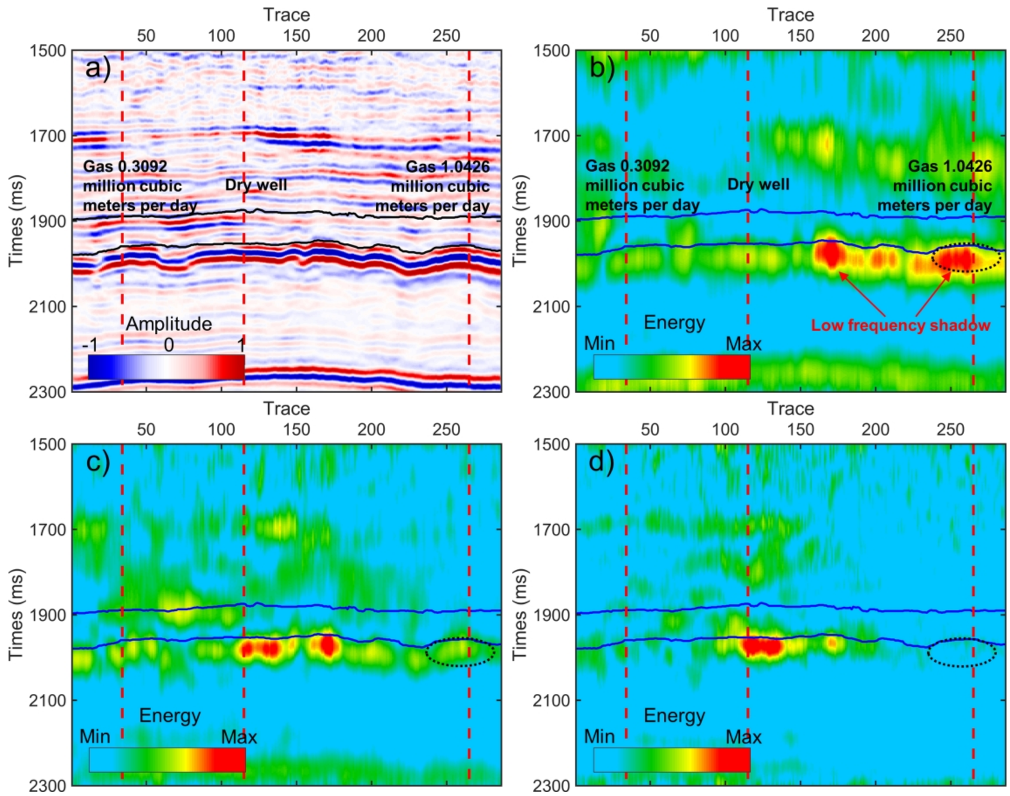

Figure 9. Post-stack seismic section (a), and S-transforms at 20 Hz (b), 30 Hz (c), and 40 Hz (d).

217x170mm (300 x 300 DPI)

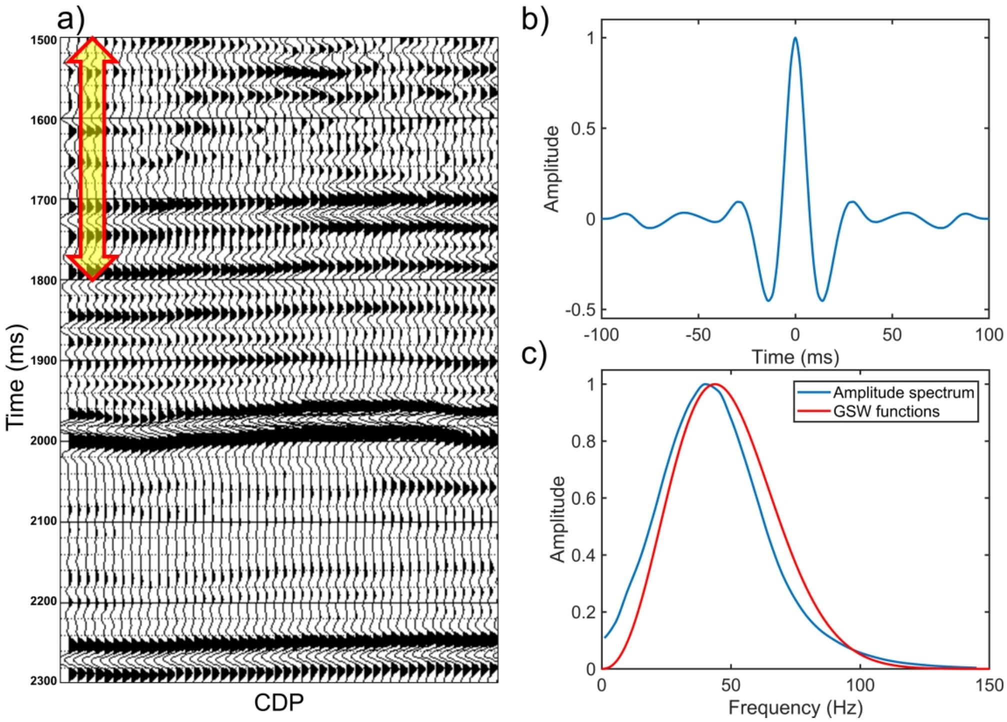

Figure 10. Post-stack seismic data (a), seismic wavelet in the time domain (b), and source wavelet amplitude spectrum fit by the GSW equation (6) (c).

264x188mm (300 x 300 DPI)

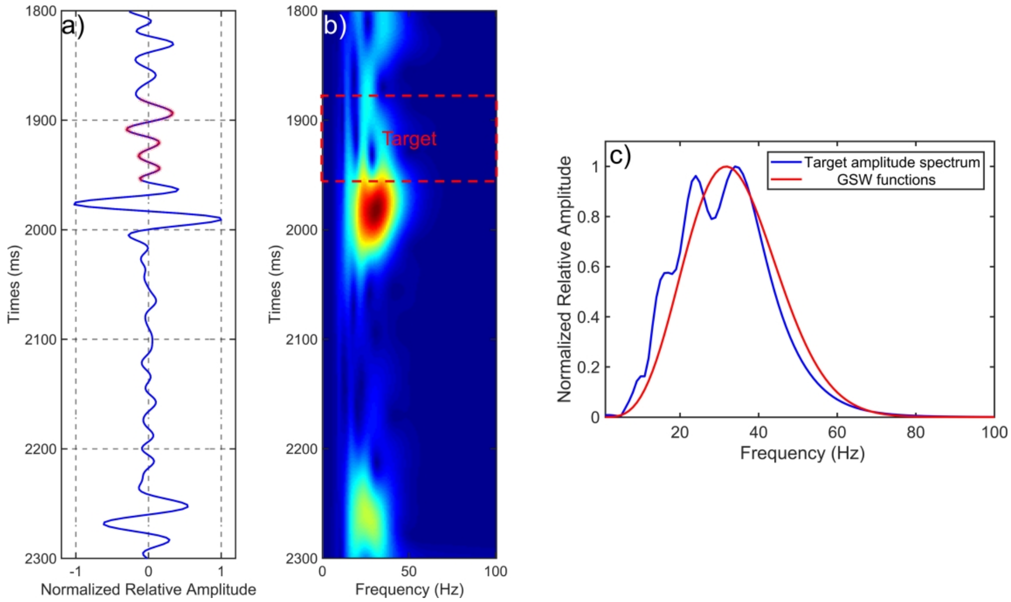

Figure 11. Single seismic trace (a), generalized S transform (b), and amplitude spectrum fit by the GSW equation (6) (c).

321x190mm (300 x 300 DPI)

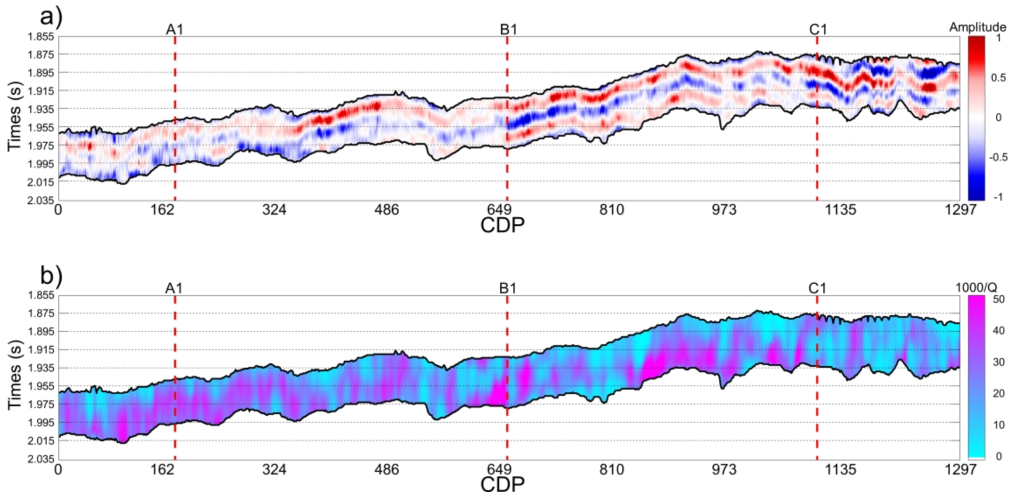

Figure 12. 2D seismic line crossing wells A1, B1 and C1. Amplitude (a) and attenuation (b) profiles.

329x160mm (300 x 300 DPI)

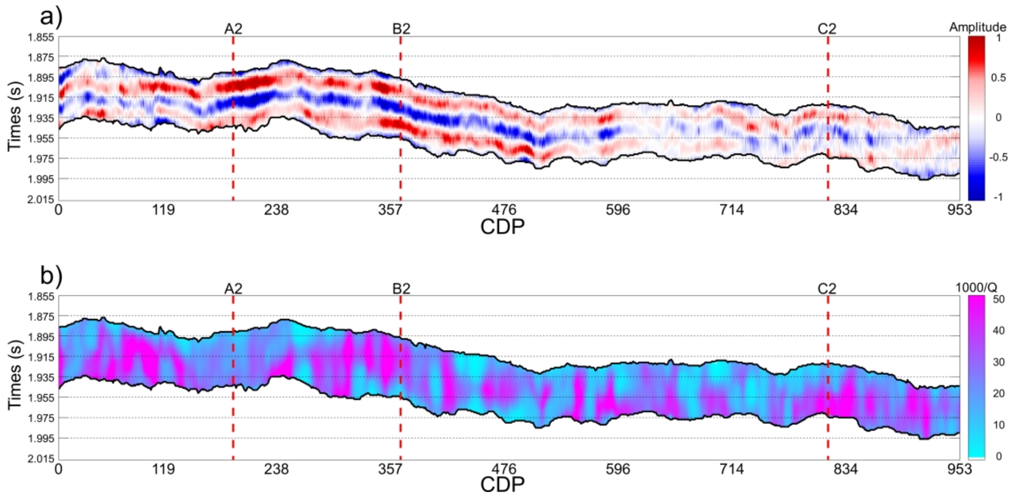

Figure 13. 2D seismic line crossing wells A2, B2 and C2. Amplitude (a) and attenuation (b) profiles.

329x160mm (300 x 300 DPI)

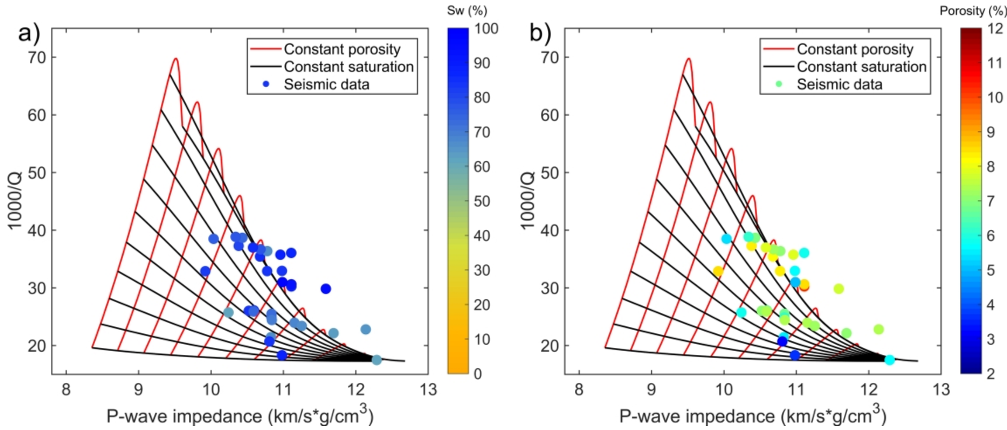

Figure 14. Seismic rock-physics interpretation template around well A.

338x142mm (300 x 300 DPI)

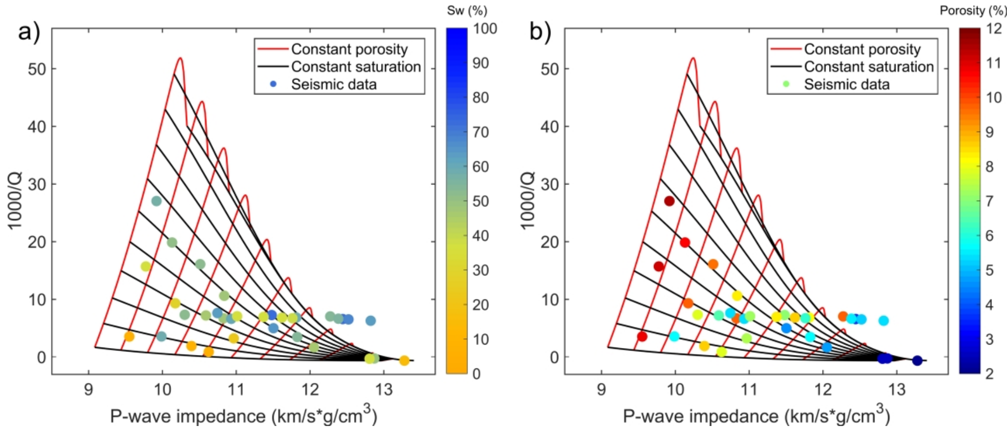

Figure 15. Seismic-rock physics interpretation template around well B.

338x142mm (300 x 300 DPI)

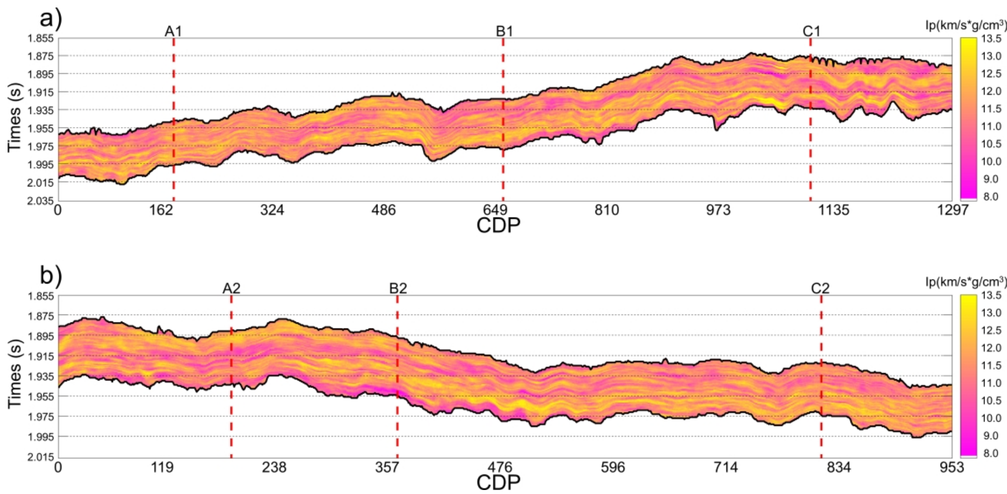

Figure 16. 2D P-wave impedance profiles crossing (a) wells A1, B1 and C1, and (b) wells A2, B2 and C2.

331x160mm (300 x 300 DPI)

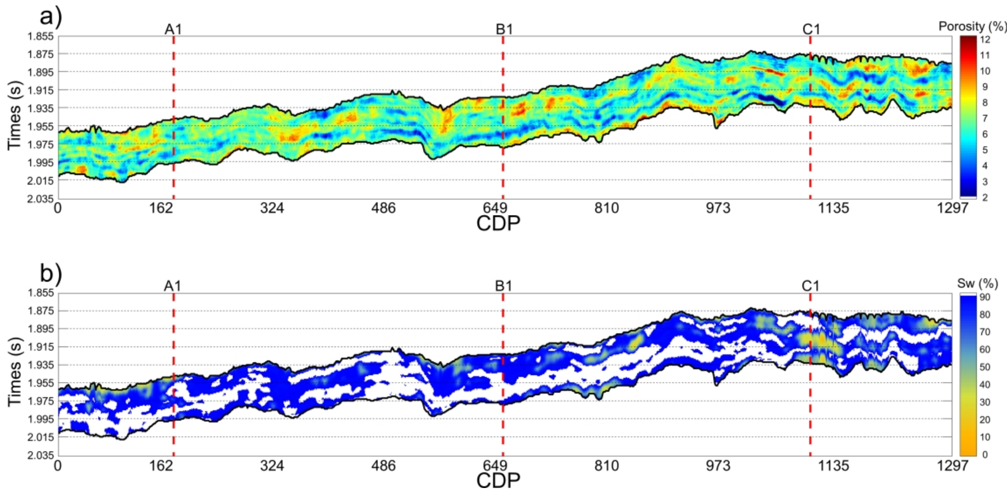

Figure 17. 2D profiles crossing wells A1, B1 and C1. (a) Porosity and (b) water saturation.

331x160mm (300 x 300 DPI)

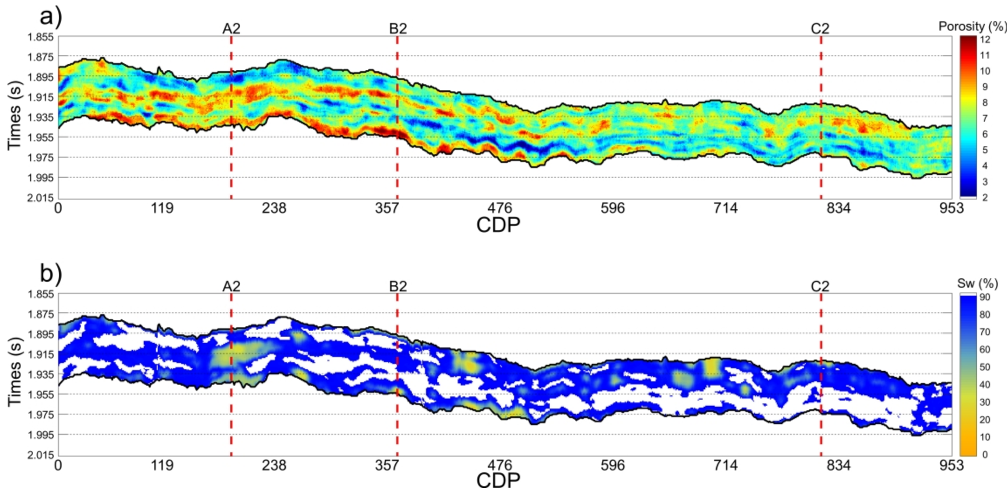

Figure 18. 2D profiles crossing wells A2, B2 and C2. (a) Porosity and (b) water saturation.

331x160mm (300 x 300 DPI)

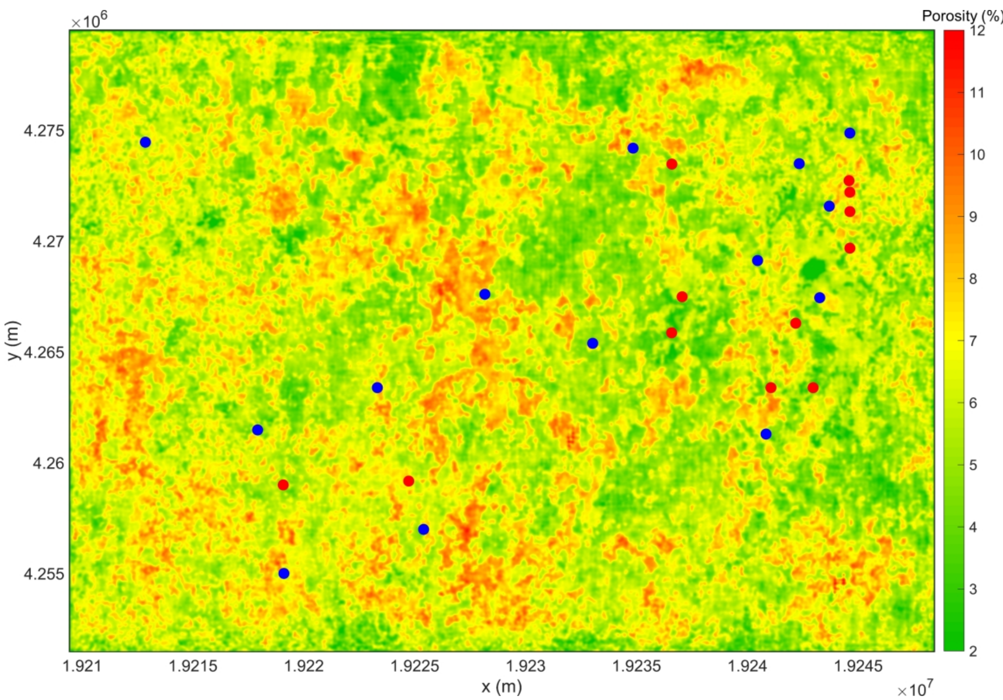

Figure 19. 3D prediction of reservoir porosity (the blue dots indicate high water saturation, and red high gas saturation).

277x190mm (300 x 300 DPI)

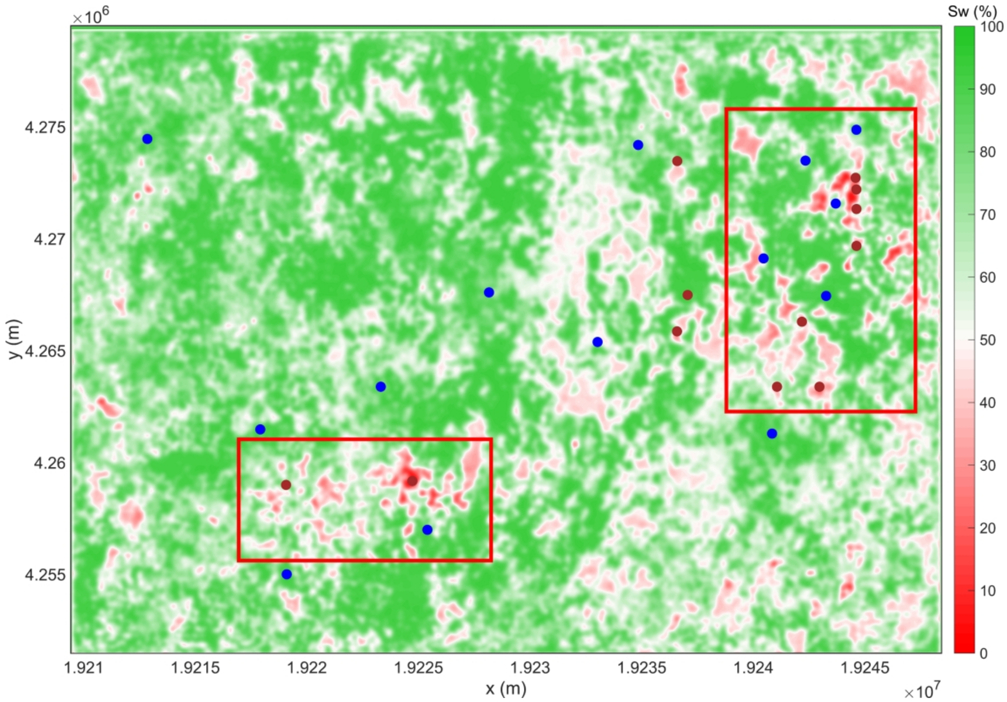

Figure 20. 3D prediction of water saturation (the blue dots indicate high water saturation, and red high gas saturation).

275x190mm (300 x 300 DPI)